




Research Article

Enhanced corrosion resistance of epoxy-films on ultra-thin SiO_x PECVD film coated laser surface melted Al-alloys

J. Varghese¹ · P. Vieth¹  · X. Xie¹ · G. Grundmeier¹

Received: 5 September 2022 / Accepted: 28 November 2022

Published online: 17 December 2022

© The Author(s) 2022 

Abstract

The influence of ultra-thin SiO_x plasma deposited films on the corrosion resistance of adhesive films on a laser surface melted 7075 aluminium alloy was investigated by means of complementary techniques in comparison to the just laser surface melted state. Laser surface melting (LSM) was performed using a continuous wave mode at a wavelength of 1064 nm. Ultra-thin plasma polymer films were deposited from a mixture of hexamethyldisilane (HMDSO), oxygen, and argon by means of an audio-frequency glow discharge. The surface morphology and surface chemistry compositions were investigated by employing field emission scanning electron microscopy, energy-dispersive X-ray spectroscopy (EDX), diffuse reflection infrared Fourier transform spectroscopy, and X-ray photoelectron spectroscopy. The corrosion resistance of plasma polymer coated LSM Al-7075 alloy was studied using linear sweep voltammetry and electrochemical impedance spectroscopy in a chloride-containing electrolyte. The electrochemical studies showed an improved corrosion resistance for plasma film-coated alloys compared to the just laser surface melted state. To study the corresponding surface adhesive properties, the samples were coated with an epoxy amine adhesive. 90°-peel test under humid conditions confirmed the improvement of interfacial wet-adhesion corrosion tests showed a strong improvement of the delamination resistance of adhesives caused by the ultra-thin interfacial SiO_x-films.

Highlights

- The combination of LSM and PECVD deposited SiO_x layers was used in order to enhance corrosion and adhesion properties
- Enhanced delamination resistance was observed through a radial corrosion process
- Surface analytical and electrochemical methods were used to examine the role of ultra-thin interfacial SiO_x films

Keywords LSM · Plasma coatings · Aluminium alloys · Corrosion resistance

Supplementary Information The online version contains supplementary material available at <https://doi.org/10.1007/s42452-022-05244-0>.

✉ P. Vieth, pfsvieth@mail.uni-paderborn.de | ¹Technical and Macromolecular Chemistry, Paderborn University, Warburgerstr. 100, 33098 Paderborn, Germany.



SN Applied Sciences

(2023) 5:29

| <https://doi.org/10.1007/s42452-022-05244-0>

1 Introduction

High-strength Aluminum 7xxx series alloys (Al–Zn–Mg–Cu) are especially applied in aerospace and automotive constructions [1, 2]. Despite its extensive application, the Al-7075 alloy is susceptible to chloride-containing electrolytes [3]. The native oxide surface film is prone to a chloride attack both under atmospheric conditions and corrosion in bulk electrolytes [4]. The EN-AW 7075 alloy is susceptible to several forms of corrosion, e.g. pitting corrosion, intergranular corrosion (IGC), and stress corrosion cracking (SCC) [5, 6]. The corrosion of this alloy is influenced by constituent particles of the alloy, interrupting the native oxide layer and serving as a defect for corrosion initiation [7–9]. While Cu and Fe lead to the formation of cathodic phases, Zn and Mg-containing phases act as local anodes [7–11]. Such constituent particles promote micro galvanic coupling and thereby pitting corrosion at the interface between the particles and the adjacent matrix.

Corrosive delamination was reported to lower macroscopic fracture toughness and thus weaken the adhesive joint at the polymer/aluminium alloy interface [12–14]. Additionally, the kinetics of electrolyte transport for interface corrosion processes for adhesive-coated metals have been studied by Posner et al. and others [12, 15–17]. They reported that the delamination rate of the adhesive is determined by the electrolyte transport at the interface polymer/aluminium alloy. In the case of polymer-coated Al 7075 alloys, corrosive delamination was reported to lower macroscopic fracture toughness and thus weaken the adhesive joint at the polymer/aluminium alloy interface [12–14].

Several surface modification processes for aluminium alloys are established, which improve the delamination resistance of aluminium alloys [18, 19].

Anodization and plasma electrolytic oxidation lead to thickened, however, porous thickened oxide films [20, 21]. In case of the anodization, such oxides form highly protective nanostructured surface layers, which are well described in several review articles [21, 22]. Chemical conversion layers substitute the oxide film with more stable oxides and phosphates e.g. titanium and zirconium [23, 24]. In addition, ultra-thin films of organosilanes and organophosphonic acids showed a strong improvement in the delamination resistance based on the combination of adhesion promotion and interfacial corrosion protection [25].

The approaches described above are based on wet-chemical processes and can typically not be applied locally. However, dry surface technologies which can be applied to locally modify an alloy e.g. in the bonding

area are highly attractive from an economic and ecologic point of view.

In this regard, laser processes and atmospheric plasma jets are of high interest [26, 27]. Laser surface melting is a well-established process in which a laser is used to heat a material to its melting point, after which it solidifies quickly [23, 24, 28, 29]. Past studies showed that various lasers like KrF excimer ($\lambda = 248$ nm, $\tau = 25$ ns), continuous 1 kW CO₂, Yb³⁺: glass fibre laser ($\lambda = 1062$ nm, $P_{\max} = 20$ W, $\tau = 230$ ns) have been used and can contribute to the corrosion resistance improvement of aluminium alloys [30–34]. The increased corrosion resistance is caused by the homogeneous surface layer compared to an unaffected alloy. Furthermore, second phase particles are dissolved and are distributed into the matrix covering the alloy from galvanic coupling and thus pitting corrosion [35]. The main parameter influencing microstructural and chemical modifications was reported to be the pulse length [36].

Laser surface treatment also can be used to improve the adhesive bonding of aluminium alloys for various reasons like uniform load distribution, increased joint stiffness, and absorption of energy [37]. Elisabeth et al. demonstrated that a good bonding surface and ageing-resistant aluminium bonded joints could be obtained via laser surface melting [38].

After laser pretreatment, Rico Rechner et al. demonstrated enhanced strength and durability in adhesive-bonded aluminium by cleaning and modifying the oxide layer [39]. The investigation by Marco Alfano et al. also demonstrated that the improvement of the aluminium-epoxy joints was due to modification of the surface chemistry of the adhesive-substrate interface using a laser ablation process [40].

Low-temperature plasma polymer deposition of thin films was shown to be a suitable process for the corrosion protection of metal alloys such as steel [41, 42], copper [43], and aluminium alloys [44]. Films deposited from the organosilane precursors by PE-CVD have been used for enhancing corrosion resistance [45]. The characteristics of films can also be tailored by the plasma deposition conditions [46].

In this work, the focus is on the corrosion protection performance of ultra-thin SiO_x films deposited by PE-CVD on laser surface melted Al-7075 alloys. The samples were analyzed by scanning electron microscopy (FE-SEM), Fourier transform infrared spectroscopy (FTIR), X-ray photoelectron spectroscopy (XPS); corrosion properties were estimated by linear sweep voltammetry (LSV), electrochemical impedance spectroscopy (EIS) and adhesion and delamination studies. A significant improvement in the resistance to corrosive delamination was observed which could be correlated to the barrier properties of the ultra-thin SiO_x films.

2 Experimental

2.1 Materials and chemicals

The material used in this study was Al-7075 alloy supplied by Rasch-Metalle GmbH & Co., Bielefeld, Germany having dimensions of 20 mm × 20 mm × 3 mm. Prior to all the experiments, the samples were mechanically wet grounded using 600, 1000, 2500, and 4000 grit silicon carbide (SiC) papers (Schmitz-Metallographie-GmbH, Germany). The samples were then rinsed with deionized water (HiPerSolv CHROMANORM Water for HPLC, VWR Chemicals, Darmstadt, Germany) and abs. ethanol (ethanol, absolute, 99.8% VWR Chemicals, Darmstadt Germany) before being dried with ultra-clean air. The abraded samples were polished with 0.3 μm Al₂O₃ powder (Schmitz GmbH & Co, Bunde, Germany) in aqueous suspension (20 g/100 ml H₂O) until a mirror-like finish was achieved. Afterwards, the samples were washed with deionized water (HiPerSolv CHROMANORM Water for HPLC, VWR Chemicals, Darmstadt, Germany) and followed by an ultrasonic bath with ethanol (ethanol, absolute, 99.8% VWR Chemicals, Darmstadt Germany) for about 30 min. Finally, samples were again dried using ultra-clean air prior to the laser surface melting (LSM) treatment.

2.2 Laser surface melting

The samples were surface melted using the Keyence MD-X1520C 3-Axis hybrid scanning laser. The marking laser is equipped with a YVO₄ laser (class 4 laser) with an output power of 25 W, and a wavelength of 1064 nm. The laser uses a continuous wave mode (CW) with a frequency range of 1–400 kHz. The temperature inside the chamber was kept under control using air-driven cooling. For this investigation, 50% of the total laser power, or 12.5 W, was chosen. The frequency of the laser and the scanning speed was 50 kHz and 700 mm/s, respectively. The melting process was done in an ambient atmosphere. The hatching distance (separation between two consecutive laser beams) was 0.06 mm, with a 0.04 mm laser track width.

2.3 PECVD of SiO_x- films

For plasma polymerization, a custom-made bell jar reactor with parallel electrodes was used. The deposition was performed with a 3.5 kHz audio frequency (af) discharge. The monomer used for the polymerization purpose was hexamethyldisiloxane (HMDSO) with a purity of 98.5% (Sigma-Aldrich). The plasma reactor was equipped with a quartz crystal microbalance (QCM) with a resonance

frequency of 5 MHz. A Cr/Au-coated AT-cut QCM crystal was used (Fil-Tech Inc., USA). QCM is an extremely sensitive mass device. The QCM provides information about the mass change (Δm) on the substrate as a function of frequency variation (Δf) [47].

Prior to the deposition, the chamber was evacuated to 10⁻⁵ mbar. During the deposition, the specimen was exposed to a gas mixture of HMDSO, oxygen, and argon. High partial pressures of oxygen lead to the deposition of SiO_x films while lower oxygen partial pressures lead to carbon and hydrogen-rich SiOCH-like films. The use of argon as a carrier gas aids in the increased fragmentation of plasma polymerization [48]. Initially, Ar was fed into the reactor at a flow rate of 0.5 ml/min and a pressure of 0.1 mbar was maintained. The partial pressure of oxygen in the vacuum chamber was then increased until it reached 0.4 mbar. Finally, the monomer partial pressure was increased to 0.45 mbar by raising the overall pressure. The plasma was ignited with a current of 1.5 mA when the chamber had reached stable pressure conditions. In this investigation, deposition times of 10 s and 20 s were used.

The mass of the deposited films as a function of frequency change before and after thin film deposition was determined using the following equation. The frequency shift, Δf = f₂ - f₁, is caused by the mass change during the deposition. f₁ and f₂ are the initial and final frequencies during the deposition. If uniform mass coverage across the surface can be assumed, the film thickness (d) can be calculated by dividing the change in mass per unit area estimated by Sauerbrey's equation by the density of film [49, 50]:

$$\Delta m = -C \cdot \frac{\Delta f}{n}$$

where C is the mass sensitivity constant related to properties of quartz and n is the number of harmonic (odd numbers). At room temperature for a 5 MHz quartz crystal, C is approximately equal to 17.7 ng cm⁻² Hz⁻¹ [51, 52]. The reported density value for the plasma polymerized films deposited using pure HMDSO and with oxygen, admixture ranges from 0.98 to 2 g/cm³ [48, 52, 53]. The thickness computed for 10 s and 20 s with a density value of 1.3 g/cm³ using the equations is 2.8 and 5.7 nm, respectively. where C is the mass sensitivity constantly related to properties of quartz and n is the number of the harmonic. At room temperature for a 5 MHz quartz crystal, C is approximately equal to 17.7 ng cm⁻² Hz⁻¹.

2.4 Chemical and morphological analysis

Field emission scanning electron microscopy (FE-SEM) imaging and EDX mapping of the samples were performed to characterize the topography and composition of the

surface and the passive layers, respectively. The imaging was performed using a NEON 40 FE-SEM microscope (Carl Zeiss SMT AG, Oberkochen, Germany), which was equipped with an InLens and an SE2 detector. The imaging was done using a 2 kV acceleration voltage. Focused ion beam (FIB) was also performed to measure the thickness of the oxide layer. FIB cuts were made using Ga liquid metal ion source (LMIS) and with a beam voltage of 30 kV.

The chemical composition of the samples was examined by Fourier transform infrared spectroscopy (FTIR). Diffuse reflection infrared spectroscopy (DRIFTS) was used for thin film characterization. A Vertex70 (Bruker) equipped with a liquid deuterated L-alanine doped triglycene sulfate (DLaTGS) detector was used to acquire the spectra. The measurements were done inside the sample compartment using a Praying Mantis™ diffuse reflectance accessory from Harrick. The spectra were averaged over 512 scans and were recorded with a spectral resolution of 4 cm^{-1} . The analysis of the spectra was done using Opus 7.0 spectroscopy software. All sample spectra were referenced to the LSM Al-7075 sample.

Additionally, X-ray photoelectron spectroscopy (XPS) was performed to study the chemical composition of as-received, polished, laser structured and SiO_x film coated samples. XPS was performed using Omicron ESCA + UHV System (Scienta Omicron NanoTechnology GmbH, Germany). The spectra were recorded with a base pressure of below 2×10^{-9} mbar, with a step size of 0.1 eV and a constant pass energy of 100 eV, with a take-off angle of 30° relative to the surface plane. The C1s signal of adventitious carbon at 284.9 eV was used as the reference binding energy scale and the spectra were fitted with the CASA XPS software (CASA Software Ltd.). For peak fitting, a Shirley background was chosen, and it was performed using a peak shape consisting of a convolution of a Gauss (30%) and Lorentzian (70%) shape. The atomic sensitivity factors supplied from Omicron were implemented in the CASA XPS database for quantification.

2.5 Electrochemical characterization

Two different types of corrosion tests had been employed in this study. Linear sweep voltammetry (LSV) and electrochemical impedance spectroscopy (EIS) tests were employed, and results of polished, laser and SiO_x deposited samples were compared. The electrochemical measurements were performed in a designed cell with a three-electrode set-up using Ag/AgCl as reference electrode (Radiometer Analytical, Hach Co. Loveland, CO, USA) and gold wire as the counter electrode. Working electrodes were Al-7075 substrates that had been prepared. A Viton O-ring was used to limit the working electrode area to 0.196 cm^2 . Corrosion testing was carried out in an aerated

borate buffer solution (0.2 mol/l H_3BO_3 , 0.05 mol/l Na_2SO_4 , 0.05 mol/l $\text{Na}_2\text{B}_4\text{O}_7 \cdot 10\text{H}_2\text{O}$, and 0.5 mol/l NaCl with a pH of 8.6. Electrochemical measurements were performed using a Reference 3000 Potentiostat (Gamry Instruments, Warminster, USA). Fresh solutions and clean electrodes and cell assembly were used in all electrochemical tests. The experimental result was fitted using origin software [54].

The potentiodynamic polarization measurements of the polished, laser surface melted and PECVD deposited specimens were performed at room temperature (25°C). Before the measurements, the open circuit potential (OCP) was measured and then the polarization curves were recorded using linear sweep voltammetry. LSV was performed from -0.1 to 0.3 V vs OCP at a scan rate of 1 mV/s and with a step size of 1 mV . The electrochemical impedance spectroscopy measurement was performed at the open circuit potential in the frequency range of 100 kHz to 0.01 Hz with a voltage perturbation of an amplitude of 10 mV . Bode plots were obtained after the specimens were immersed in the test solution for a duration of 20 h . All EIS measurements were carried out at room temperature (25°C).

The equivalent circuits (EC) presented in Figure S10 were used for fitting procedure of the obtained impedance data. The EC presented in (a) is simulating the impedance of an oxide covered Al-alloy according to [55]. R_{elec} represents the resistance of the electrolyte, R_{po} the resistance of the oxide layer, R_b the resistance of the barrier layer, CPE_{po} and CPE_b (Constant Phase Element), with the fitting parameter n , ranging from 0 to 1 with 1 as an ideal capacitor was used in order to obtain more precise results. [55] The EC presented in (b) was used for the fitting procedure of the SiO_x covered samples, whereas R_{elec} represents the resistance of the electrolyte, R_b the resistance of the barrier layer and CPE_b as Constant Phase Element in order to obtain more precious results.

2.6 Peel test studies

For the adhesive and delamination studies, a two-component hot-cured amine-epoxy resin adhesive was employed as the model polymer film. The adhesive mixture consists of epoxy resin D.E.R. 331 (Dow Chemicals) and amine hardener Jeffamin D400 (Sigma-Aldrich). These were mixed well until it became clear. It's then stirred for 10 min in a vacuum at 130 rpm with a magnetic stir bar. The mixture was then degassed in a vacuum for 1 h without mixing, followed by 15 min of ultrasonication at ambient temperature. Finally, the adhesive mixture was again degassed in a vacuum for 1 h .

Adhesive tapes were used as spacers in the samples to obtain a homogenous adhesive layer thickness. For this

purpose, the samples were taped with 'Magic tape' (3 M, Germany GmbH) as the first layer and 5 layers with TESA films (TESA), as shown in Figure S1. The amine-epoxy resin adhesive was carefully poured onto the sample surfaces under a dry atmosphere (< 8% RH) and placed on polytetrafluorethylene (PTFE) blocks covered with Al foil to form a sandwich geometry. The joint was fastened with clips and cured for 75 min at 120 °C. When the samples were cooled down to room temperature, the clamps were removed. After hardening, the aluminium foil was pulled off without disturbing the adhesive, leaving a pore-free free-standing adhesive film. The adhesive-applied samples were kept in a closed chamber with a water-filled beaker at 40 °C. This procedure leads to the saturation of epoxy-amine films with water.

For the peel test experiment, an MV-220 (Imada, Japan) motorized test setup was used. The test was conducted in a humid atmosphere (> 95% r.h.) at a constant angle perpendicular to the substrate surface. The peel force was measured by a ZP-5 force gauge (Imada, Japan). The speed of the gauge was set at 1 mm/s. The program (ZP recorder) records 1000 measured points/s. The plateau area of the force–displacement curves was only considered while evaluating or averaging the force.

2.7 Corrosion tests

For measuring the radial corrosion propagation at the interface, an artificial defect was applied using a milling machine at the centre of the samples with a diameter of 1 mm. These samples were immersed in a 3.5% NaCl solution for 9 days in a humidified environment (> 95% r.h.) maintained at 40 °C. Each day, the radial corrosion progress starting from the defect was imaged with help of an optical microscope (Olympus SZX16).

3 Results and discussions

3.1 Surface chemical and morphological analysis

The FE-SEM images of the laser-melted Al-7075 are depicted in Fig. 1. The laser tracks and protrusions on the surface are visible. The laser-melted surfaces exhibit a wavy morphology in the form of ripples. These ripples are attributed to the surface tension of the melt pool and the shear stress produced from the surface tension gradients [56]. Under this condition, a radial temperature gradient is

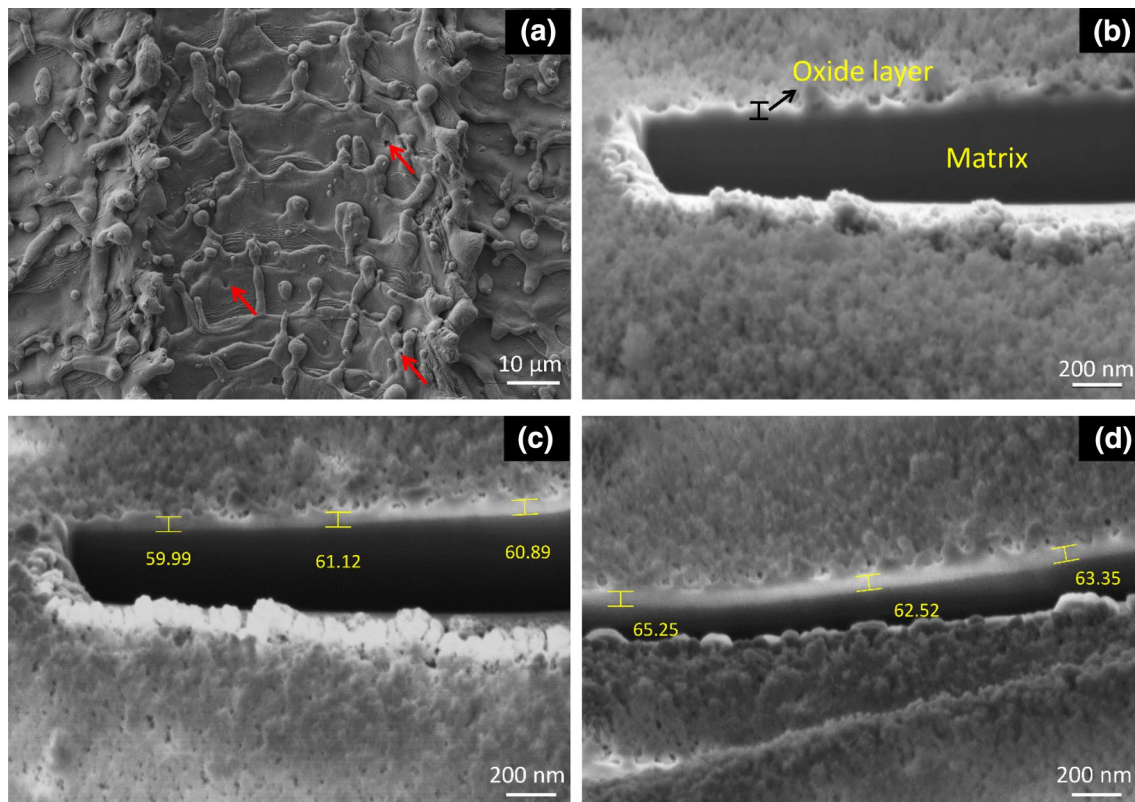


Fig. 1 SEM images for laser surface melted Al-7075 samples. **a** Shows the top-view of the LSM sample and **b** shows the cross-sectional view of the FIB cut after LSM, **c** and **d** show FIB cuts of plasma

films coated samples (deposition times: **c** 10 s and **d** 20 s). The red arrows in **(a)** point to the presence of micropores on the surface after LSM

generated, which pulls back the melted liquid away from the centre to the adjacent areas by the surface tension gradient, thereby reducing the surface of liquid under the beam and heightening the surrounding area (Marangoni flow) [57]. Due to the large temperature gradient and rapid solidification, the pulled liquid solidifies at the edges creating a wavy-like morphology.

Once the temperature of the surface reaches vaporization temperature, large thermal stresses can be induced. This may introduce defects such as micro-pores by evaporation of elements like magnesium and zinc that have a boiling temperature lower than the temperature that results from the laser. Red arrows in Fig. 1a indicate the presence of pores on the surface. The presence of such pores can reduce the corrosion resistance of the treated sample. The cross-sectional view of the LSM Al-7075 sample Fig. 1b shows an average surface oxide layer thickness of about 57.5 ± 3.1 nm.

Figure 1c, d shows the FE-SEM images with FIB cut after plasma deposition for a duration of 10 s and 20 s, respectively. The average total oxide thickness after deposition was higher than for the LSM sample. Figure S1 shows FE-SEM images of (a) 3 nm SiO_x and (b) 6 nm SiO_x . Scale bar 10 μm .

The determined overall oxide thickness as measured by FIB-SEM was 60.5 ± 1.4 nm for 10 s and 64.1 ± 1.6 nm for the 20 s treated samples. Considering the laser-formed oxide layer thickness of 57.5 ± 3.1 nm, the deposited SiO_x -film thickness was about 3 nm for the 10 s deposition time and 6.6 nm for the 20 s deposition time.

When comparing the oxide thickness on the LSM sample and after SiO_x film deposition, the results are in very good agreement with the QCM thickness measurements. The variation of change in mass calculated using the Sauerbrey equation at different deposition times is also shown as a graphical representation in Fig. 2. The thickness calculation was based on an assumed SiO_x density of 1.3 g/cm^3 . The given data shown in Fig. 2 predict a linear increasing thickness dependent on the deposition time.

3.2 DRIFTS analysis

The analysis of the PECVD SiO_x film as deposited on the laser-melted aluminium surface was performed using FTIR DRIFTS spectroscopy. Figure 3 shows the DRIFTS data of the deposited SiO_x films on LSM Al-7075 samples for a thickness of 3 nm and 6 nm. From the spectra of the deposited samples, the characteristic features for the Si–O stretching vibration of the Si–O–Si bond were identified around 1060 cm^{-1} [58, 59]. The similar

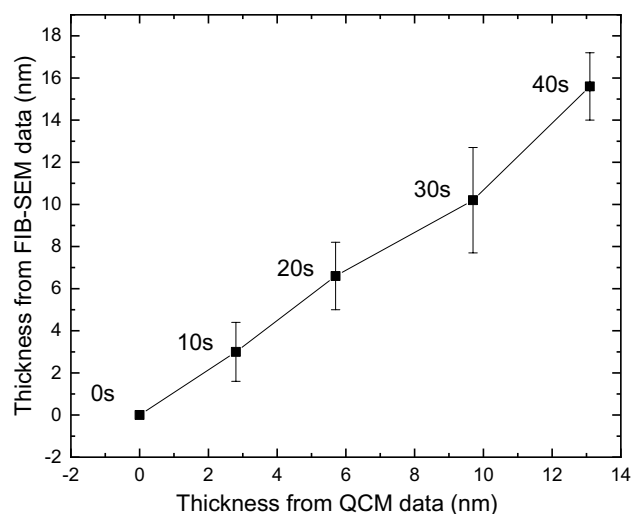


Fig. 2 Graphical representation showing the variation of thickness of deposited SiO_x films on LSM Al alloys as a function of deposition times (measured using QCM set-up) and thickness measurements via FIB-SEM

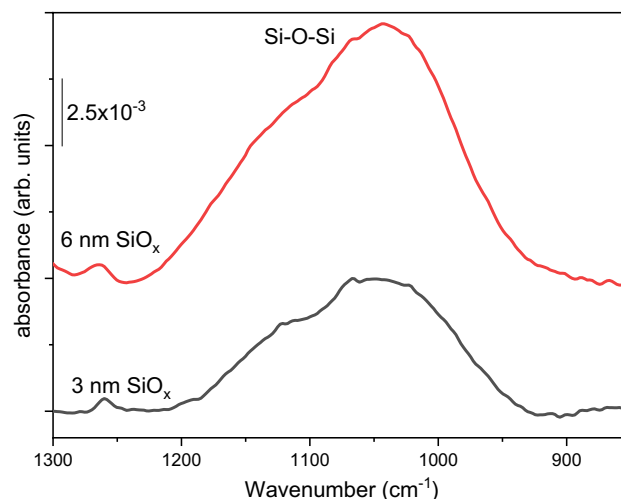


Fig. 3 DRIFTS data of plasma deposited ultra-thin SiO_x films (3 nm and 6 nm) on LSM Al 7075. The LSM Al 7075 sample was used as a reference

peak shape for both thickness values indicates that the crosslinking did not vary with the growth of the SiO_x film.

From the spectra of the deposited samples, the characteristic features for Si–O stretching vibration of the Si–O–Si bond were identified around 1060 cm^{-1} [58, 59]. In comparison to a recent publication of de los Arcos et al. discussing the FTIR analysis of porous and

dense Si–O–Si, both films are rather defect-rich [60]. We assume that this is due to the very rough substrate surface.

3.3 XPS analysis of the surface composition

The chemical composition of the surface of SiO_x with a film thickness of 3 and 6 nm deposited samples were studied by XPS in comparison to the just laser surface melted substrate. Table 1 shows the total chemical composition as determined via survey quantification.

The LSM-Al 7075 sample showed a thickened oxide layer due to high-temperature oxidation during the LSM process showing the oxidic component at 74.2 eV of the Al 2p peak while the metallic contribution is completely diminished. The deposition of the SiO_x films is revealed by the concentration of Si 2p and the SiO_x component of the O 1 s peak at 532.2 eV and 532.5 eV. The SiO_x concentration is strongly increased for the 6 nm deposition whereas the oxidic and hydroxylic components of the oxyhydroxide layer decreased. The overall increased Si content for the 6 nm sample confirms the SiO_x film deposition.

The survey spectrum of the two deposited samples with SiO_x films is presented in the supplementary information (Figure S2). Core level spectra for Si 2p, O 1 s, C 1 s, and Al 2p are shown in Fig. 4. The derived atomic compositions and peak positions based on the peak fittings are listed in Table 2. The O 1 s signal of the two samples with deposited SiO_x films consists of three components. The peak observed at 532.5 eV was assigned to SiO_x (O–Si) [61], while the peaks around 532 eV [62] and around 530 eV were attributed to oxyhydroxides (AlOOH) and oxides (Al₂O₃), respectively [63].

For the fitting of Si 2p peaks, the two components (Si 2p_{3/2} and Si 2p_{1/2}) of the spin–orbit doublet were considered according to the literature [64–66]. The distance between the two components was fixed at 0.6 eV, with a ratio (2p_{1/2}:2p_{3/2}) of 1:2. The slight shift of Si 2p peak

positions is attributed to an enhanced concentration of Si^{IV} states in the film [64]. Figure 4c, f shows the Al 2p high-resolution spectra of the deposited samples. It was assigned as one component with a binding energy between 74.3 and 74.5 eV, correlating with aluminium oxide. Although a few nanometers of SiO_x are deposited onto the laser surface melted aluminium alloy, there is still a significant Al concentration visible. A defect-rich oxide layer in the LSM state is assumed, whereas the SiO_x is deposited in the pores and acts as an effective barrier film.

3.4 Electrochemical analysis

Figure 5 shows the Tafel plots of the different samples as measured by linear sweep voltammetry (LSV). The black curve corresponds to the polished sample and the red curve to the LSM sample surface. The blue and green curves show the data for the SiO_x films as deposited on the laser surface melted samples. The corrosion potential (E_{corr}) and the associated corrosion current density (i_{corr}) were determined by the tangent method for each curve. The polished Al-7075 sample surface exhibits a corrosion potential of $-0.24 \text{ V}_{\text{SHE}}$ and a corrosion current density of $7.85 \times 10^{-4} \text{ mA/cm}^2$ and was chosen as reference.

The laser surface melted sample shows a cathodic shift of -0.2 V in comparison to the polished state which can be explained by strong inhibition of the cathodic current density.

The SiO_x film-covered surfaces show an additional lowering of the cathodic current densities and in addition inhibition of the anodic dissolution rate. As expected, the 6 nm film shows an improved barrier property in comparison to the just 3 nm thin film leading to the most significant lowering of the anodic corrosion rate. As it is shown elsewhere, the LSM procedure leads to a nonporous oxide layer [55]. As described above, the deposition of the SiO_x films result in an anodic shift of the corrosion potential and a reduction of the corrosion current density based on the inhibition of the anodic dissolution rate. The SiO_x films are acting as a barrier film and are closing defects in the nanoporous oxide film.

Electrochemical Impedance spectroscopy (EIS) was used to further characterize the corrosion properties of bare and coated Al-alloy substrates. Figure 6 depicts the time-dependent magnitude and phase plots of the samples measured during the immersion in 0.05 M chloride-containing borate buffer electrolyte.

The equivalent circuits (EC) used for the fitting procedure are shown in Figure S9. The measurements

Table 1 Surface chemical composition determined via XPS survey quantification in the laser surface melted state and additionally covered with a 3 nm and a 6 nm PECVD SiO_x-film

| Element | SiO _x 3 nm | SiO _x 6 nm | LSM-Al 7075 |
|---------|-----------------------|-----------------------|-------------|
| | At. % | At. % | At. % |
| Al 2p | 31.6 | 24.7 | 24.1 |
| O 1 s | 48.9 | 51.8 | 49.7 |
| C 1 s | 13.5 | 9.6 | 26.2 |
| Si 2p | 6 | 13.9 | – |

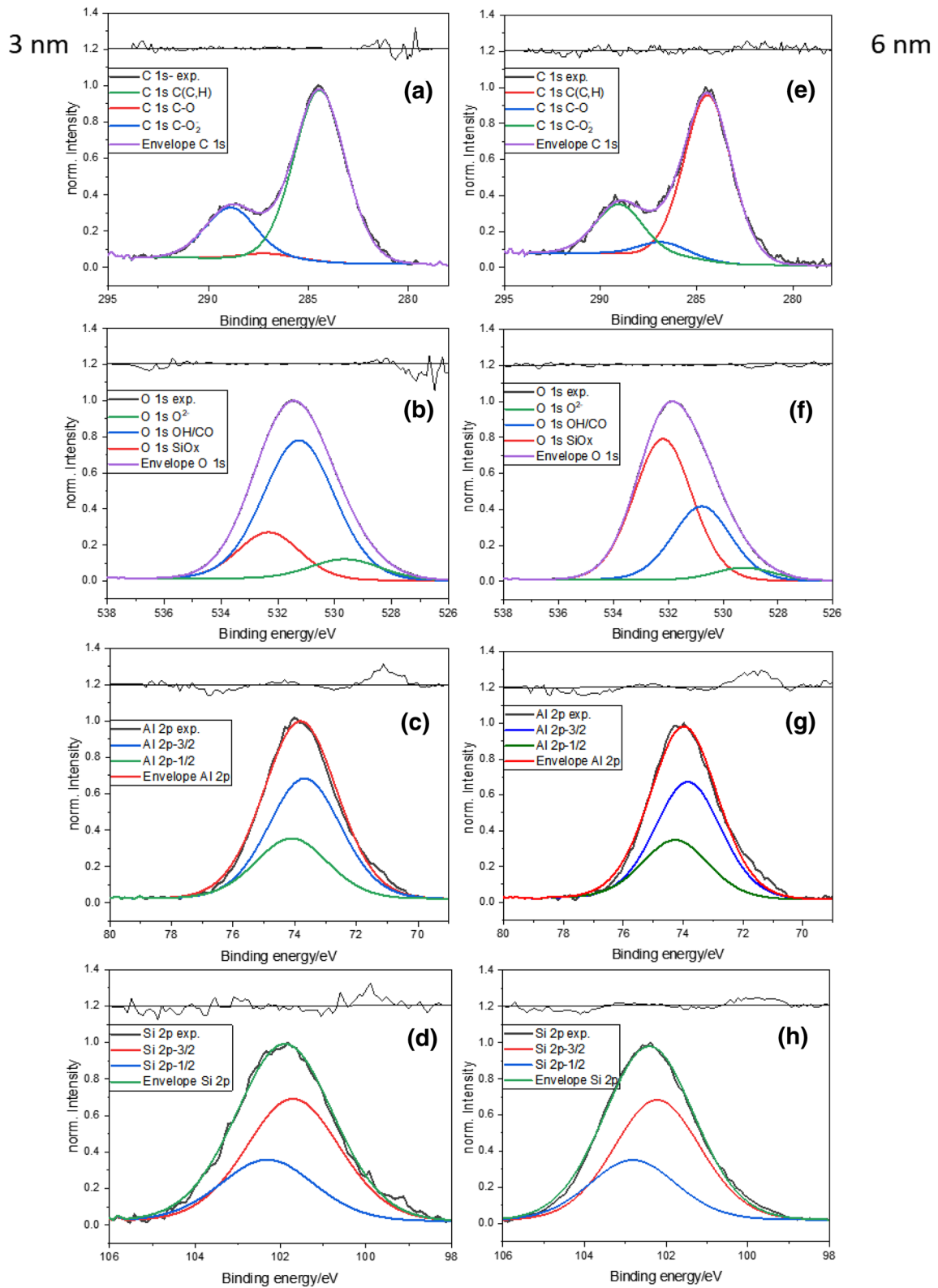


Fig. 4 XPS high-resolution spectra of C 1 s, O 1 s, Si 2p and Al 2p of the deposited SiO_x film on the laser surface melted Al-substrate (**a-d** d=3 nm and **e-h** d=6 nm)

Table 2 Atomic concentrations of the surfaces in the laser surface melted state and additionally covered with a 3 nm and a 6 nm thin PECVD SiO_x film as derived from high-resolution element spectra

| Element (XPS peak) | Chemical structure | SiO _x (d=3 nm) | | SiO _x (d=6 nm) | | LSM-Al 7075 | |
|--------------------|--------------------------------|---------------------------|------|---------------------------|------|-------------|------|
| | | BE (eV) | At.% | BE (eV) | At.% | BE (eV) | At.% |
| O 1 s | SiO _x | 532.3 | 9.8 | 532.2 | 32.2 | – | – |
| | AlOOH | 531.3 | 33.8 | 531.5 | 16.9 | 531.8 | 27.7 |
| | Al ₂ O ₃ | 529.7 | 5 | 529.9 | 3 | 530.4 | 22 |
| C 1 s | Aliphatic | 284.5 | 10.1 | 284.5 | 6.9 | 284.5 | 20.2 |
| | C–O | 287.1 | 0.3 | 286.8 | 0.6 | 286.9 | 2.3 |
| | CO ₂ [–] | 288.9 | 3 | 289 | 2 | 288.8 | 3.7 |
| Si 2p | SiO _x | 101.9 | 6 | 102.4 | 14 | – | – |
| Al 2p | Oxidic | 74.3 | 31.8 | 74.5 | 24.4 | 74.2 | 24.1 |

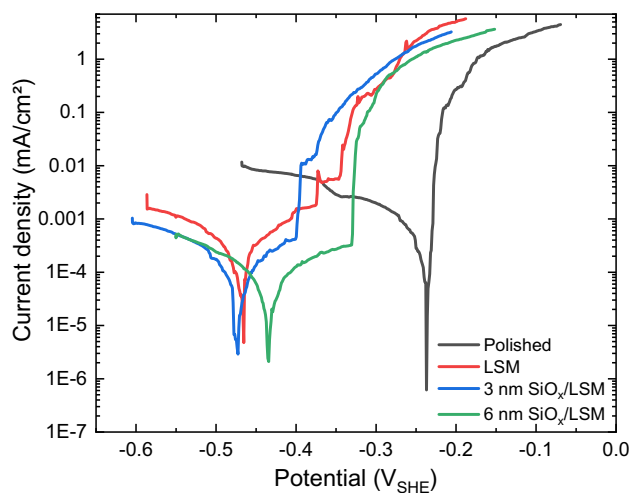


Fig. 5 Results of linear sweep voltammetry of the studied samples in borate buffer with 0.05 M chloride (pH 8.6)

were performed over an immersion time of 18 h. Regarding the quantitative evaluation of the parameters, it is important to consider that especially for the bare Al-alloy substrates, the chloride induced corrosion leads to non-stationary conditions, which are not incorporated in the theoretical approach. Table S1 summarizes the relevant data based on the fitting procedure of the EIS data. Figure 6c indicates significant higher impedance values in the initial phase of immersion after the LSM procedure, which is attributed to the formed oxide [55]. Figure 6c, f show the impedance values for the 3 nm and 6 nm SiO_x thin film covered samples. It is observed, that the deposition of such SiO_x layers lead to a significant increase in corrosion resistance. The 6 nm thin film shows an even increased corrosion protection compared to the SiO_x film with a thickness of 3 nm. The analysis of the corresponding R_p values (impedance at 0.01 Hz) as shown in Figure 7 as function of time illustrated the related transients. The highly crosslinked SiO_x films act as an effective barrier

films for chloride ions and thereby enhance the corrosion resistance. The relevant Nyquist plots are shown in Figure S10.

However, even in the presence of the thin PECVD SiO_x films the low-frequency region indicates active corrosion which leads to the conclusion that pores within the PECVD film act as active sites for a corrosive attack. However, the low-frequency impedance is increased by at least an order of magnitude by the thin SiO_x films indicating a good coverage of the rough LSM sample (Fig. 7).

3.5 Analysis of adhesion properties and corrosive delamination

The interfacial adhesion properties of different modified surfaces in combination with a reference epoxy amine resin were investigated by means of peel test measurements under humid conditions. The peel forces measured after four weeks of wet exposure are presented in Fig. 8. Measurements on polished and LSM Al-7075 samples resulted in peel forces of 0.2 ± 0.1 and 2.2 ± 0.6 N/mm, respectively. The ten-fold increase in peel force on the LSM sample indicates the effect of mechanical interlocking on the observed adhesion forces. A FE-SEM picture after a FIB-Cut is given in Figure S6 in order to present the obtained microstructure after the LSM procedure. For the SiO_x film-coated Al-7075 samples, increased peel forces were obtained. For the SiO_x coated samples, even cohesive fracture of the adhesive films was observed (Figure S8).

The comparison of the delamination kinetics of different samples immersed in 3.5% NaCl solution is shown in Fig. 9. Severe corrosive delamination could be observed for the polished alloy while the LSM Al-7075 already showed an inhibition of the delamination process.

The additional deposition of the two thin SiO_x films led to significant inhibition of the corrosive delamination.

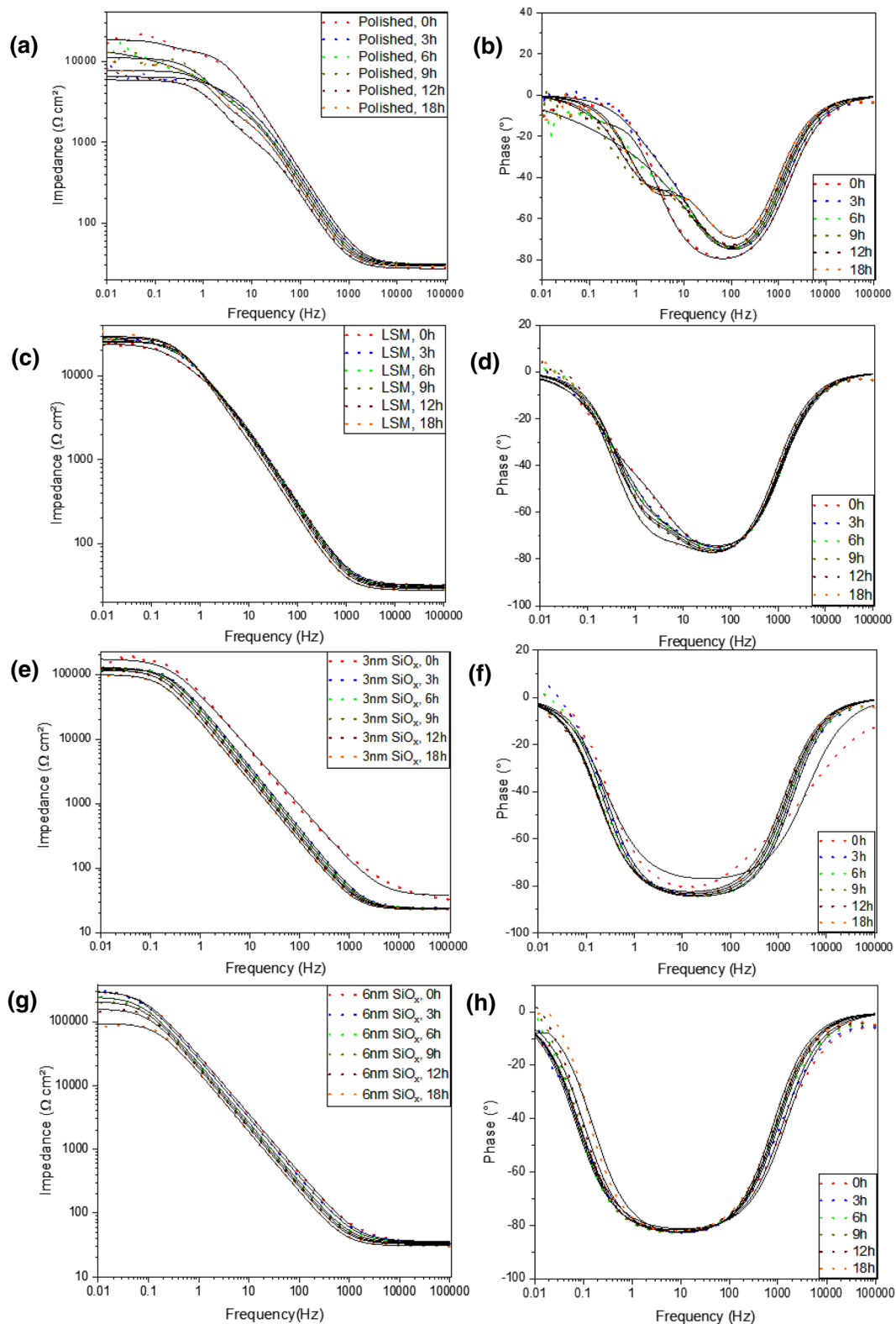


Fig. 6 Time-dependent plots of electrochemical impedance measurements of the studied samples in borate buffer with 0.05 M chloride (pH 8.6). Plots are given for **a** polished Al 7075 Impedance and **b** Phase plots polished Al 7075, **c** LSM-7075 Impedance, and

d Phase plots LSM-7075, **e** 3 nm SiO_x deposited film Impedance, and **f** Phase plots 3 nm SiO_x deposited film, **g** 6 nm deposited film Impedance and **h** Phase plots 6 nm deposited film

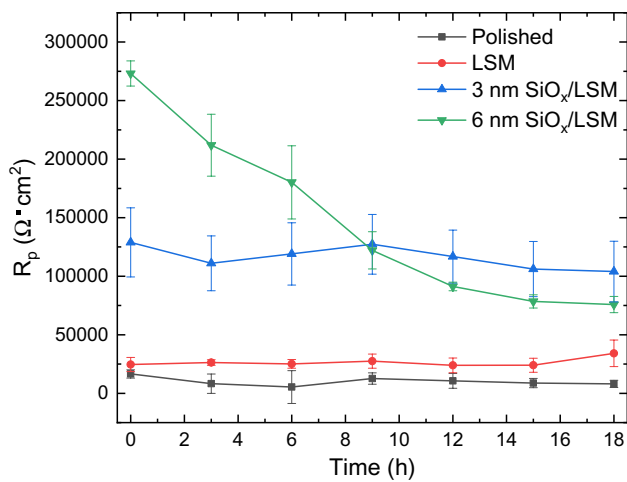


Fig. 7 Polarization resistance as a function of time of immersion for the different samples

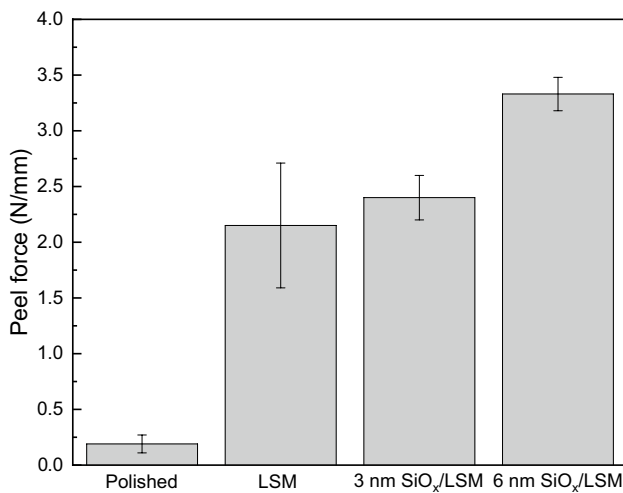


Fig. 8 90°-peel forces measured in a humid atmosphere on the polished and LSM Al-7075 alloy surfaces coated with epoxy-amine adhesive

Within the studied time range no difference between the two film thickness values was observed. The results show that the electrochemical measurements could well predict the resulting increased corrosion resistance of the polymer/alloy interface.

Figure 10 summarizes the average delamination rates for various sets of samples. The delaminated area and the average radial progress were evaluated. A linear increase of the delamination rate indicates that the reaction kinetics and not transport kinetics determine the corrosive delamination [67].

4 Conclusions

It could be shown that the corrosive delamination resistance of laser surface melted Al-7075 alloys can be strongly enhanced by the deposition of ultra-thin SiO_x PECVD films. FTIR DRIFTS and XPS analysis proved the formation of a SiO_x thin film formation on the rough surface oxide. As shown by LSV and EIS studies, both the cathodic reduction of oxygen and anodic dissolution rates could be strongly reduced by ultra-thin SiO_x films. However, the increase of the thickness from 3 to 6 nm led to a further decrease of the anodic dissolution rates based on the higher surface coverage and reduced defect density. The wet-adhesion strength of an epoxy-based adhesive as measured by peel-tests under humid conditions could be increased mainly by the LSM treatment which is assigned to interfacial mechanical interlocking. However, a further improvement could be achieved by the deposition of ultra-thin SiO_x films, which might be due to an increase of the hydrolytic stability of the oxide phase underneath the adhesive film. The strongly inhibited corrosive delamination of the applied adhesive film could be explained as mainly based on the inhibition of interfacial electrochemical reaction kinetics. The comparison of the electrochemical results for the thin film coated surfaces and the corrosion studies of epoxy coated surfaces illustrated that the residual defects in the plasma thin films which lead to a localized corrosive attack are of minor importance for the delamination process at the adhesive/ SiO_x /oxide/alloy interface. This conclusion is of importance for the application of plasma thin film deposition for such systems as a defect-free plasma thin film under industrial conditions is hard to achieve.

Fig. 9 Optical microscope images showing the propagation of corrosive delamination of different samples as a function of time

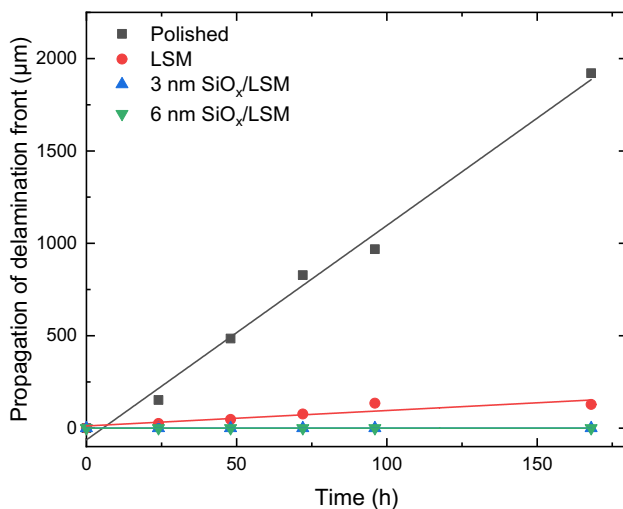
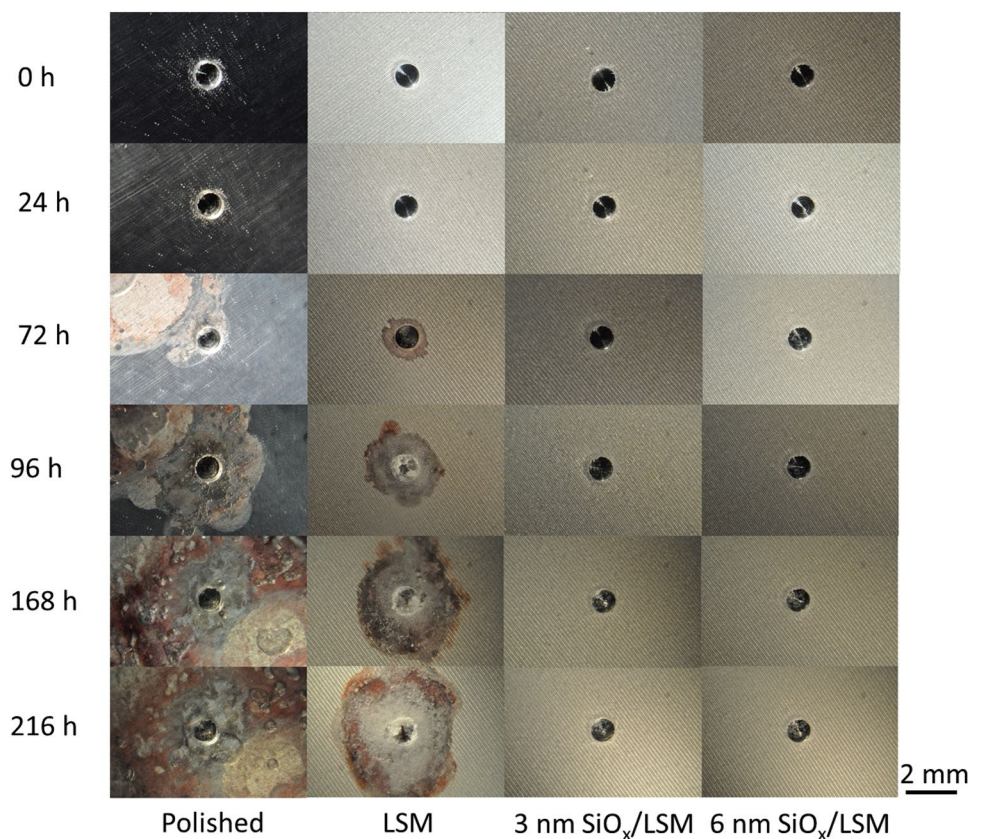


Fig. 10 Progress of the delamination front as a function of time for the different surface treatments

Acknowledgements The authors would like to acknowledge the German Research Foundation (Deutsche Forschungsgemeinschaft, DFG) for the financial support (Project No. 409784234; GR 1709/26-1) and (Project No. 138690629; GR TRR 87/3). In addition, we thank Nadine Buitkamp (Department of Coating Materials & Polymers, Paderborn University, Paderborn, Germany) for the FE-SEM and FIB measurements.

Author contribution CRediT authorship contribution statement: JV: Investigation, Formal analysis, Data Curation PV: Conceptualization, Data Curation, Formal analysis, Investigation, Validation. Writing-original draft; XX: Formal analysis, Investigation; GG: Conceptualization, Supervision, Validation, Writing Review & Editing, Funding acquisition.

Funding Open Access funding enabled and organized by Projekt DEAL.

Declarations

Conflict of interest The authors declare that there is no conflict of interest.

Open Access This article is licensed under a Creative Commons Attribution 4.0 International License, which permits use, sharing, adaptation, distribution and reproduction in any medium or format, as long as you give appropriate credit to the original author(s) and the source, provide a link to the Creative Commons licence, and indicate if changes were made. The images or other third party material in this article are included in the article's Creative Commons licence, unless indicated otherwise in a credit line to the material. If material is not included in the article's Creative Commons licence and your intended use is not permitted by statutory regulation or exceeds the permitted use, you will need to obtain permission directly from the copyright holder. To view a copy of this licence, visit <http://creativecommons.org/licenses/by/4.0/>.

References

1. Birbilis N, Buchheit RG (2008) Investigation and discussion of characteristics for intermetallic phases common to aluminum alloys as a function of solution pH. *J Electrochem Soc* 155(3):C117. <https://doi.org/10.1149/1.2829897>
2. Hirsch J, Skrotzki B, Gottstein G (2008) Aluminium alloys: their physical and mechanical properties. In: Proceedings of the 11th international conference on aluminium alloys, 22–26 Sept. 2008, Aachen, Germany; ICAA 11. Wiley-VCH, Weinheim
3. Polmear I (2017) Light alloys: metallurgy of the light metals. Butterworth-Heinemann, Oxford
4. Noor EA (2009) Potential of aqueous extract of Hibiscus sabdariffa leaves for inhibiting the corrosion of aluminum in alkaline solutions. *J Appl Electrochem* 39(9):1465–1475. <https://doi.org/10.1007/s10800-009-9826-1>
5. Benedetti A, Cabeza M, Castro G, Feijoo I, Mosquera R, Merino P (2012) Surface modification of 7075-T6 aluminium alloy by laser melting. *Surf Interface Anal* 44(8):977–981. <https://doi.org/10.1002/sia.4840>
6. Sankaran KK, Perez R, Jata KV (2001) Effects of pitting corrosion on the fatigue behavior of aluminum alloy 7075-T6: modeling and experimental studies. *Mater Sci Eng A* 297(1–2):223–229. [https://doi.org/10.1016/S0921-5093\(00\)01216-8](https://doi.org/10.1016/S0921-5093(00)01216-8)
7. Padovani C, Davenport AJ, Connolly BJ, Williams SW, Siggs E, Groso A et al (2011) Corrosion protection of AA7449-T7951 friction stir welds by laser surface melting with an Excimer laser. *Corros Sci* 53(12):3956–3969. <https://doi.org/10.1016/j.corsci.2011.07.043>
8. Hu B, Richardson IM (2007) Microstructure and mechanical properties of AA7075(T6) hybrid laser/GMA welds. *Mater Sci Eng A* 459(1–2):94–100. <https://doi.org/10.1016/j.msea.2006.12.094>
9. Sajadifar SV, Scharifi E, Weidig U, Steinhoff K, Niendorf T (2020) Effect of tool temperature on mechanical properties and microstructure of thermo-mechanically processed AA6082 and AA7075 aluminum alloys. *HTM J Heat Treat Mater* 75(3):177–191. <https://doi.org/10.3139/105.110412>
10. Sajadifar SV, Scharifi E, Weidig U, Steinhoff K, Niendorf T (2020) Performance of thermo-mechanically processed AA7075 alloy at elevated temperatures—from microstructure to mechanical properties. *Metals* 10(7):884. <https://doi.org/10.3390/met10070884>
11. Starink MJ (2001) Effect of compositional variations on characteristics of coarse intermetallic particles in overaged 7000 aluminium alloys. *Mater Sci Technol* 17(11):1324–1328. <https://doi.org/10.1179/026708301101509449>
12. Cavezza F, Boehm M, Terryn H, Hauffman T (2020) A review on adhesively bonded aluminium joints in the automotive industry. *Metals* 10(6):730. <https://doi.org/10.3390/met10060730>
13. Guo S, Carlson BE, Hector LG, Xia Y, Zhou Q (2018) Increasing strength and fracture toughness of AA7075-T6 adhesively bonded joints with laser ablation. *J Mater Process Technol* 259:368–379. <https://doi.org/10.1016/j.jmatprotec.2018.05.010>
14. Maleki HN, Chakherlou TN (2017) Investigation of the effect of bonded composite patch on the mixed-mode fracture strength and stress intensity factors for an edge crack in aluminum alloy 2024-T3 plates. *J Reinf Plast Compos* 36(15):1074–1091. <https://doi.org/10.1177/0731684417702001>
15. Posner R, Giza G, Vlasak R, Grundmeier G (2009) In situ electrochemical Scanning Kelvin Probe Blister-Test studies of the de-adhesion kinetics at polymer/zinc oxide/zinc interfaces. *Electrochim Acta* 54(21):4837–4843. <https://doi.org/10.1016/j.electacta.2009.03.089>
16. Posner R, Fink N, Wolpers M, Grundmeier G (2013) Electrochemical electrolyte spreading studies of the protective properties of ultra-thin films on zinc galvanized steel. *Surf Coat Technol* 228:286–295. <https://doi.org/10.1016/j.surfcoat.2013.04.042>
17. Posner R, Wapner K, Stratmann M, Grundmeier G (2009) Transport processes of hydrated ions at polymer/oxide/metal interfaces. *Electrochim Acta* 54(3):891–899. <https://doi.org/10.1016/j.electacta.2008.06.074>
18. Vargel C, Germain J-M (2020) Corrosion of aluminium. Elsevier Science, Amsterdam
19. Yahalom J (2011) Corrosion protection methods. *Encycl Mater Sci Technol*. <https://doi.org/10.1016/B0-08-043152-6/00306-5>
20. Zaraska L, Sulka GD, Szeremeta J, Jaskuła M (2010) Porous anodic alumina formed by anodization of aluminum alloy (AA1050) and high purity aluminum. *Electrochim Acta* 55(14):4377–4386. <https://doi.org/10.1016/j.electacta.2009.12.054>
21. Lee W, Park S-J (2014) Porous anodic aluminum oxide: anodization and templated synthesis of functional nanostructures. *Chem Rev* 114(15):7487–7556. <https://doi.org/10.1021/cr500002z>
22. Paz Martínez-Viademonte M, Abrahami ST, Hack T, Burchardt M, Terryn H (2020) A review on anodizing of aerospace aluminum alloys for corrosion protection. *Coatings* 10(11):1106. <https://doi.org/10.3390/coatings10111106>
23. Zhan W, Qian X, Gui B, Liu L, Liu X, Li Z et al (2020) Preparation and corrosion resistance of titanium–zirconium–cerium based conversion coating on 6061 aluminum alloy. *Mater Corros* 71(3):419–429. <https://doi.org/10.1002/maco.201911193>
24. Milošev I, Frankel GS (2018) Review—conversion coatings based on zirconium and/or titanium. *J Electrochem Soc* 165(3):C127–C144. <https://doi.org/10.1149/2.0371803jes>
25. Wapner K, Stratmann M, Grundmeier G (2008) Structure and stability of adhesion promoting aminopropyl phosphonate layers at polymer/aluminium oxide interfaces. *Int J Adhes Adhes* 28(1–2):59–70. <https://doi.org/10.1016/j.ijadhadh.2007.05.001>
26. Penkov OV, Khadem M, Lim W-S, Kim D-E (2015) A review of recent applications of atmospheric pressure plasma jets for materials processing. *J Coat Technol Res* 12(2):225–235. <https://doi.org/10.1007/s11998-014-9638-z>
27. Saleema N, Gallant D (2013) Atmospheric pressure plasma oxidation of AA6061-T6 aluminum alloy surface for strong and durable adhesive bonding applications. *Appl Surf Sci* 282:98–104. <https://doi.org/10.1016/j.apsusc.2013.05.064>
28. Steen WM, Mazumder J, Mazumder J (2010) Laser material processing, 4th edn. Springer, London
29. Ion JC (2005) Laser processing of engineering materials: Principles, procedure and industrial application, 1st edn. Elsevier/Butterworth-Heinemann, Amsterdam
30. Dahotre NB, Harimkar SP (2008) Laser fabrication and machining of materials. Springer, New York
31. Bonora PL, Bassoli M, Anna P, Battaglin G, Della Mea G, Mazzoldi P et al (1980) Electrochemical and corrosion behaviour of laser modified aluminium surfaces. *Electrochim Acta* 25(11):1497–1499. [https://doi.org/10.1016/0013-4686\(80\)87168-4](https://doi.org/10.1016/0013-4686(80)87168-4)
32. Yue T, Yan L, Chan C, Dong C, Man H, Pang G (2004) Excimer laser surface treatment of aluminum alloy AA7075 to improve corrosion resistance. *Surf Coat Technol* 179(2–3):158–164. [https://doi.org/10.1016/S0257-8972\(03\)00850-8](https://doi.org/10.1016/S0257-8972(03)00850-8)
33. Mroczkowska KM, Antończak AJ, Gąsiorek J (2019) The corrosion resistance of aluminum alloy modified by laser radiation. *Coatings* 9(10):672. <https://doi.org/10.3390/coatings9100672>
34. Pinto MA, Cheung N, Ierardi MCF, Garcia A (2003) Microstructural and hardness investigation of an aluminium–copper alloy processed by laser surface melting. *Mater Charact* 50(2–3):249–253. [https://doi.org/10.1016/S1044-5803\(03\)00091-3](https://doi.org/10.1016/S1044-5803(03)00091-3)

35. Li R, Ferreira M, Almeida A, Vilar R, Watkins KG, McMahon MA et al (1996) Localized corrosion of laser surface melted 2024-T351 aluminium alloy. *Surf Coat Technol* 81(2–3):290–296. [https://doi.org/10.1016/0257-8972\(95\)02484-0](https://doi.org/10.1016/0257-8972(95)02484-0)
36. Pou-Álvarez P, Riveiro A, Nóvoa XR, Fernández-Arias M, Del Val J, Comesaña R et al (2021) Nanosecond, picosecond and femtosecond laser surface treatment of magnesium alloy: role of pulse length. *Surf Coat Technol* 427:127802. <https://doi.org/10.1016/j.surfcoat.2021.127802>
37. Wu Y, Lin J, Carlson BE, Lu P, Balogh MP, Irish NP et al (2016) Effect of laser ablation surface treatment on performance of adhesive-bonded aluminum alloys. *Surf Coat Technol* 304:340–347. <https://doi.org/10.1016/j.surfcoat.2016.04.051>
38. Stammen E, Dilger K, Böhm S, Hose R (2007) Surface modification with laser: pretreatment of aluminium alloys for adhesive bonding. *Plasma Process Polym* 4(S1):S39–S43. <https://doi.org/10.1002/ppap.200730303>
39. Rechner R, Jansen I, Beyer E (2010) Influence on the strength and aging resistance of aluminium joints by laser pre-treatment and surface modification. *Int J Adhes Adhes* 30(7):595–601. <https://doi.org/10.1016/j.ijadhadh.2010.05.009>
40. Alfano M, Pini S, Chiodo G, Barberio M, Pirondi A, Furguele F et al (2014) Surface patterning of metal substrates through low power laser ablation for enhanced adhesive bonding. *J Adhes* 90(5–6):384–400. <https://doi.org/10.1080/00218464.2013.871538>
41. Shirtcliffe N, Thiemann P, Stratmann M, Grundmeier G (2001) Chemical structure and morphology of thin, organo-silicon plasma-polymer films as a function of process parameters. *Surf Coat Technol* 142–144:1121–1128. [https://doi.org/10.1016/S0257-8972\(01\)01226-9](https://doi.org/10.1016/S0257-8972(01)01226-9)
42. Vautrin-UI C, Roux F, Boisse-Laporte C, Pastol JL, Chausse A (2002) Hexamethyldisiloxane (HMDSO)-plasma-polymerised coatings as primer for iron corrosion protection: influence of RF bias. *J Mater Chem* 12(8):2318–2324. <https://doi.org/10.1039/B111509J>
43. Lin Y, Yasuda H (1996) Effect of plasma polymer deposition methods on copper corrosion protection. *J Appl Polym Sci* 60(4):543–555. [https://doi.org/10.1002/\(SICI\)1097-4628\(19960425\)60:4%3c543:AID-APP8%3e3.0.CO;2-O](https://doi.org/10.1002/(SICI)1097-4628(19960425)60:4%3c543:AID-APP8%3e3.0.CO;2-O)
44. Grundmeier G, Stratmann M (1998) Plasma polymerization—a new and promising way for the corrosion protection of steel. *Mater Corros* 49(3):150–160. [https://doi.org/10.1002/\(SICI\)1521-4176\(199803\)49:3%3c150:AID-MACO150%3e3.0.CO;2-X](https://doi.org/10.1002/(SICI)1521-4176(199803)49:3%3c150:AID-MACO150%3e3.0.CO;2-X)
45. Domingues L, Oliveira C, Fernandes J, Ferreira M (2002) EIS on plasma-polymerised coatings used as pre-treatment for aluminium alloys. *Electrochim Acta* 47(13–14):2253–2258. [https://doi.org/10.1016/S0013-4686\(02\)00064-6](https://doi.org/10.1016/S0013-4686(02)00064-6)
46. Yu QS, Reddy CM, Moffitt CE, Wieliczka DM, Johnson R, Deffeyes JE et al (2000) Improved corrosion protection of aluminum alloys by system approach interface engineering: part 2—AA2024-T3. *Corrosion* 56(9):887–900. <https://doi.org/10.5006/1.3280592>
47. Zhang J, Ji X, Bao J, Zheng X (2016) Deposition and characterization of Si-doped diamond films using tetraethoxysilane onto a WC-Co substrate. *Coatings* 6(3):39. <https://doi.org/10.3390/coatings6030039>
48. Posner R, Santa M, Grundmeier G (2011) Wet- and corrosive de-adhesion processes of water-borne epoxy film coated steel. *J Electrochem Soc* 158(3):C29. <https://doi.org/10.1149/1.3525239>
49. Böke F, Giner I, Keller A, Grundmeier G, Fischer H (2016) Plasma-enhanced chemical vapor deposition (PE-CVD) yields better hydrolytical stability of biocompatible SiO_x thin films on implant alumina ceramics compared to rapid thermal evaporation physical vapor deposition (PVD). *ACS Appl Mater Interfaces* 8(28):17805–17816. <https://doi.org/10.1021/acsami.6b04421>
50. Sauerbrey G (1959) Verwendung von Schwingquarzen zur Wgung dner Schichten und zur Mikrowgung. *Z Physik* 155(2):206–222. <https://doi.org/10.1007/BF01337937>
51. Huang X, Bai Q, Hu J, Hou D (2017) A practical model of quartz crystal microbalance in actual applications. *Sensors (Basel)*. <https://doi.org/10.3390/s17081785>
52. Huang X, Chen Q, Pan W, Hu J, Yao Y (2019) Assessing the mass sensitivity for different electrode materials commonly used in quartz crystal microbalances (QCMs). *Sensors (Basel)*. <https://doi.org/10.3390/s19183968>
53. Boutamine M, Lezzar OC, Bellel A, Aguir K, Sahli S, Raynaud P (2018) Determination of volatile organic compounds using quartz crystal microbalances coated with hexamethyldisiloxane. *Anal Lett* 51(3):387–400. <https://doi.org/10.1080/00032719.2017.1339356>
54. OriginLab—Origin and OriginPro—Data analysis and graphing software. [July 28, 2022]. <https://www.originlab.com/>
55. Vieth P, Garthe M-A, Voswinkel D, Schaper M, Grundmeier G (2022) Enhancement of the delamination resistance of adhesive film coated surface laser melted aluminum 7075-T6 alloy by aminophosphonic acid adsorption. *Surf Coat Technol* 447:128835. <https://doi.org/10.1016/j.surfcoat.2022.128835>
56. Moffitt CE, Reddy CM, Yu QS, Wieliczka DM, Johnson R, Deffeyes JE et al (2000) Improved corrosion protection of al alloys by system approach interface engineering: part 3—AA7075-T6. *Corrosion* 56(10):1032–1045. <https://doi.org/10.5006/1.3294380>
57. Anthony TR, Cline HE (1977) Surface rippling induced by surface-tension gradients during laser surface melting and alloying. *J Appl Phys* 48(9):3888–3894. <https://doi.org/10.1063/1.324260>
58. Hegemann D, Vohrer U, Oehr C, Riedel R (1999) Deposition of SiO_x films from O₂/HMDSO plasmas. *Surf Coat Technol* 116–119:1033–1036. [https://doi.org/10.1016/S0257-8972\(99\)00092-4](https://doi.org/10.1016/S0257-8972(99)00092-4)
59. Creatore M, Palumbo F, d’Agostino R (2002) Deposition of SiO_x films from hexamethyldisiloxane/oxygen radiofrequency glow discharges: process optimization by plasma diagnostics. *Plasma Polym* 7(3):291–310. <https://doi.org/10.1023/A:1019942625607>
60. de los Arcos T, Müller H, Wang F, Damerla VR, Hoppe C, Weinberger C et al (2021) Review of infrared spectroscopy techniques for the determination of internal structure in thin SiO₂ films. *Vib Spectrosc* 114:103256. <https://doi.org/10.1016/j.vibspec.2021.103256>
61. Grothe R, Wiesing M, Giner I, Meinderink D, Grundmeier G (2017) Scanning Kelvin probe blister studies of the delamination of epoxy films on organosilane modified ZnMgAl alloy coated steel. *Mater Corros* 68(12):1314–1320. <https://doi.org/10.1002/maco.201709462>
62. Giza M, Thissen P, Grundmeier G (2008) Adsorption kinetics of organophosphonic acids on plasma-modified oxide-covered aluminum surfaces. *Langmuir* 24(16):8688–8694. <https://doi.org/10.1021/la8000619>
63. Azioune A, Marozzi M, Revello V, Pireaux J-J (2007) Deposition of polysiloxane-like nanofilms onto an aluminium alloy by plasma polymerized hexamethyldisiloxane: characterization by XPS and contact angle measurements. *Surf Interface Anal* 39(7):615–623. <https://doi.org/10.1002/sia.2563>
64. Hoppe C, Mitschker F, Butterling M, Liedke MO, de Los Arcos T, Awakowicz P et al (2020) Characterisation of micropores in

- plasma deposited SiO_x films by means of positron annihilation lifetime spectroscopy. *J Phys D Appl Phys* 53(47):475205. <https://doi.org/10.1088/1361-6463/aba8ba>
65. Alexander MR, Short RD, Jones FR, Michaeli W, Blomfield CJ (1999) A study of HMDSO/O₂ plasma deposits using a high-sensitivity and -energy resolution XPS instrument: curve fitting of the Si 2p core level. *Appl Surf Sci* 137(1–4):179–183. [https://doi.org/10.1016/S0169-4332\(98\)00479-6](https://doi.org/10.1016/S0169-4332(98)00479-6)
66. Grundmeier G, Stratmann M (1995) Nucleation and growth of plasma-polymerised hexamethyldisilazane on iron-substrates. *Ber Bunsenges Phys Chem* 99(11):1387–1392. <https://doi.org/10.1002/bbpc.199500090>
67. Wapner K, Stratmann M, Grundmeier G (2005) Application of the Scanning Kelvin Probe for the study of the corrosion resistance of interfacial thin organosilane films at adhesive/metal interfaces. *Silicon Chem* 2(5–6):235–245. <https://doi.org/10.1007/s11201-005-0935-3>

Publisher's Note Springer Nature remains neutral with regard to jurisdictional claims in published maps and institutional affiliations.